Petroleum Science 21 (2024) 1852–1864

Contents lists available at ScienceDirect

Petroleum Science

journal homepage: www.keaipublishing.com/en/journals/petroleum-science

Original Paper

# Proppant transport in rough fracture networks using supercritical $CO_2$

Yong Zheng [a, b], Meng-Meng Zhou [c], Ergun Kuru [d], Bin Wang [c], Jun Ni [e], Bing Yang [a], Ke Hu [d], Hai Huang [a, b, **], Hai-Zhu Wang [c, *]

[a] School of Petroleum Engineering, Xi'an Shiyou University, Xi'an, 710065, Shaanxi, China
[b] Shaanxi Key Laboratory of Carbon Dioxide Sequestration and Enhanced Oil Recovery, Xi'an, 710075, Shaanxi, China
[c] State Key Laboratory of Petroleum Resources and Engineering, China University of Petroleum (Beijing), Beijing, 102249, China
[d] School of Mining and Petroleum Engineering, University of Alberta, Edmonton, T6G 2W2, Alberta, Canada
[e] Shaanxi Yanchang Petroleum (Group) Co., Ltd., Xi'an, 710075, Shaanxi, China

ARTICLE INFO

*Article history:*
Received 27 December 2023
Received in revised form
4 February 2024
Accepted 27 March 2024
Available online 29 March 2024

Edited by Meng-Jiao Zhou

*Keywords:*
Reservoir stimulation
CCUS
Rough fracture network
Supercritical $CO_2$
Proppant transport

ABSTRACT

Proppant transport within fractures is one of the most critical tasks in oil, gas and geothermal reservoir stimulation, as it largely determines the ultimate performance of the operating well. Proppant transport in rough fracture networks is still a relatively new area of research and the associated transport mechanisms are still unclear. In this study, representative parameters of rough fracture surfaces formed by supercritical $CO_2$ fracturing were used to generate a rough fracture network model based on a spectral synthesis method. Computational fluid dynamics (CFD) coupled with the discrete element method (DEM) was used to study proppant transport in this rough fracture network. To reveal the turning transport mechanism of proppants into branching fractures at the intersections of rough fracture networks, a comparison was made with the behavior within smooth fracture networks, and the effect of key pumping parameters on the proppant placement in a secondary fracture was analyzed. The results show that the transport behavior of proppant in rough fracture networks is very different from that of the one in the smooth fracture networks. The turning transport mechanisms of proppant into secondary fractures in rough fracture networks are gravity-driven sliding, high velocity fluid suspension, and fracture structure induction. Under the same injection conditions, supercritical $CO_2$ with high flow Reynolds number still has a weaker ability to transport proppant into secondary fractures than water. Thickening of the supercritical $CO_2$ needs to be increased beyond a certain value to have a significant effect on proppant carrying, and under the temperature and pressure conditions of this paper, it needs to be increased more than 20 times (about 0.94 mPa s). Increasing the injection velocity and decreasing the proppant concentration facilitates the entry of proppant into the branching fractures, which in turn results in a larger stimulated reservoir volume. The results help to understand the proppant transport and placement process in rough fracture networks formed by reservoir stimulation, and provide a theoretical reference for the optimization of proppant pumping parameters in hydraulic fracturing.


## 1. Introduction

With the growing demand for oil and gas and the gradual depletion of conventional hydrocarbon resources, unconventional oil and gas resources, such as shale oil and gas, are becoming increasingly important in global oil exploration and production (Dou et al., 2022).The common characteristics of unconventional oil and gas reservoirs are their extremely low porosity and permeability, which result in high fluid flow resistance (Yuan and Wood, 2018; Zhang et al., 2021b). This necessitates reservoir stimulation to improve the reservoir permeability in order to achieve economic development. Hydraulic fracturing is the most widely used reservoir stimulation technique, which increases the connectivity area between the wellbore and the reservoir, thereby significantly enhancing hydrocarbon productivity.

Water-based fracturing fluid is currently the most extensively used working fluid in hydraulic fracturing (Davoodi et al., 2023).

* Corresponding author.
** Corresponding author.
*E-mail addresses:* huanghai@xsyu.edu.cn (H. Huang), whz0001@126.com (H.-Z. Wang).

https://doi.org/10.1016/j.petsci.2024.03.023

However, studies have indicated that water-based fracturing fluid may not be the optimal working fluid for improving recovery rates in unconventional reservoirs (Hyman et al., 2016; Middleton et al., 2014, 2017; Wang et al., 2018b), and it faces challenges associated with environmental risks and water resource consumption (Estrada and Bhamidimarri, 2016; Jackson et al., 2014; Vengosh et al., 2014; Vidic et al., 2013; Zhang and Yang, 2015). In response to these limitations, supercritical $CO_2$ has emerged as an alternative waterless fracturing fluid, exhibiting significant potential. Compared to traditional water-based fracturing fluid, the use of supercritical $CO_2$ as a working fluid can significantly enhance oil and gas recovery, reduces consumption of water resources, and facilitate carbon sequestration to effectively promote carbon emission reduction (Haq et al., 2023; Middleton et al., 2015; Mojid et al., 2021; Song et al., 2019; Yang et al., 2022). The promising prospects of supercritical $CO_2$ fracturing have led to a growing interest in related research in recent years.

The transport and placement of proppant within the fractures is a critical issue in reservoir stimulation, as it largely determines the ultimate performance of the operated well (Roostaei et al., 2020). Extensive production data and experiments on fractured wells have demonstrated a strong correlation between well performance and the quantity of added proppant (Ahamed et al., 2021; Coulter et al., 2004; King, 2010). To accurately predict the distribution of proppant within fractures, numerous researchers have conducted extensive theoretical, experimental, and numerical simulation studies in recent years. Initially, artificial fractures were assumed to be single planar fractures, which simplified the characterization of the basic morphological features of hydraulic fractures and thus became widely used in proppant transport research. The interaction between proppant particles and fluid within a single planar fracture was analyzed theoretically, considering factors such as fluid rheology, injection velocity, perforation location, fracture width, proppant particle size, proppant density, and proppant concentration (Barboza et al., 2021; Isah et al., 2021; Li et al., 2023; Roostaei et al., 2020; Yao et al., 2022; Zeng et al., 2019; Zhang et al., 2021a). These investigations revealed the controlling physics behind proppant transport behavior and its mechanisms, leading to the development of empirical relationships to predict proppant placement distance and height within single planar fractures.

The interaction between hydraulic fractures and natural fractures, bedding planes, and other geological heterogeneities in the reservoir forms a complex fracture network during fracturing treatments (Cipolla et al., 2008), and the low viscosity of supercritical $CO_2$ further increases the complexity of the fractures (Yang et al., 2022; Zhang et al., 2017), posing challenges for the effective placement of proppant throughout the entire fracture network. Complex fracture networks generated by hydraulic fracturing in unconventional reservoirs often consist of multiple-stage fractures, such as primary, secondary, and tertiary fractures. The transport and distribution of proppant within these multi-stage fracture networks are critical and can impact the ultimate oil recovery. Most studies on proppant transport in fracture networks assume a smooth surface for each level of fractures due to the complex physical processes involved in proppant transport (Sahai and Moghanloo, 2019). In complex fracture networks composed of smooth planar fractures, proppant enters secondary fractures through two mechanisms: at low fluid velocities, proppant falls from the primary fracture under the influence of gravity, while at high fluid velocities, proppant is suspended and enters branching fractures (Sahai et al., 2014). The efficiency of proppant entry into secondary fractures depends on the complexity of the fracture network and the combined effects of injection velocity, proppant concentration, and proppant size (Li et al., 2023; Sahai and Moghanloo, 2019; Tong and Mohanty, 2016; Wang et al., 2018a). Additionally, in smooth fracture network, the complexity of fractures is not the main limiting factor as long as a sufficient amount of proppant is injected (Alotaibi and Miskimins, 2018), but the variation in proppant pathways at the intersection points of the fracture network increases the risk of bridging (Kou et al., 2019).

For the transport behavior of supercritical $CO_2$-carrying proppant within the single planar fracture, the researchers found in their experiments that the proppant dune equilibrium height correlates significantly with the supercritical $CO_2$ fluid Reynolds number (Zheng et al., 2022b). Lowering the $CO_2$ injection temperature, increasing the injection displacement and using smaller proppant sizes help to obtain better proppant placement (Liu et al., 2024; Zheng et al., 2020). In the single fracture with rough wall, when the ratio of particle diameter to average fracture width is not more than 0.4, supercritical $CO_2$ carrying proppant can be able to get better transporting effect in the rough fracture (Zheng et al., 2023), and the efficient pumping scheme of supercritical $CO_2$ slurry is given (Sun et al., 2018; Zheng et al., 2021). For the flow of supercritical $CO_2$ slurry in a smooth fracture network, it was found that turbulence occurs behind the fracture junction which promotes the entry of proppant into secondary fractures, and that the low viscosity of supercritical $CO_2$ enhances the bridging effect on secondary fractures (Wang et al., 2018a; Zhang et al., 2023).

The actual stimulation fracture network is characterized by tortuous and rough surfaces, which introduces additional complexities to the transport behavior of proppant compared to smooth surfaces. Moreover, there are no reported studies investigating the turning transport mechanism of proppants into branching fractures within a rough fracture network, whether in water-based fracturing fluids or supercritical $CO_2$. This knowledge gap hampers the industry's understanding of the actual transport behavior of proppant in underground artificially complex fracture networks. There is still much speculation regarding how proppant can be effectively transported from primary fractures to secondary fractures, which hinders the design of hydraulic fracturing treatments and optimization of key pumping parameters.

To date, there are no experimental reports in the literature on supercritical $CO_2$-carrying proppant transport within rough fractures, and the use of simulations to investigate this is a potential future trend. Numerical simulation methods for proppant transport are mainly classified into two categories, i.e., Eulerian-Eulerian and Eulerian-Lagrangian (Isah et al., 2021). The Eulerian-Eulerian method treats the proppant particles as a continuous medium, which is widely used in proppant transport simulations due to its low computational effort (Wang, 2020), but it cannot be used at the particle scale to reveal the mechanisms behind the phenomena, such as proppant bridging. Whereas in Eulerian-Lagrangian methods, such as the computational fluid dynamics (CFD) coupled discrete element method (DEM), the fluid phase is considered as a continuous medium while the proppant is considered as a discrete particle, which is able to take into account particle-particle, particle-fluid, and particle-wall interactions, and is therefore considered to be a very promising method to study the characteristics and mechanisms of proppant and fluid flow (Wang et al., 2022, 2023).

The purpose of this study is to elucidate the turning transport behavior of proppants within a rough fracture network formed during reservoir stimulation, which closely approximates the actual conditions of proppant transport in artificial fracture networks. Initially, we constructed a complex fracture network with rough surfaces based on the characteristics of fractures induced by supercritical $CO_2$ fracturing. Subsequently, a validated CFD-DEM model was employed to numerically investigate the transport of proppants within the rough fracture network. By comparing the proppant transport behavior in smooth fracture networks, this

study reveals the turning transport mechanism of proppants into branching fractures at the intersections of rough fracture networks. Furthermore, the impacts of fluid viscosity, injection velocity, and proppant concentration on proppant entry into branching fractures are investigated.

## 2. Methodology

### 2.1. Construction of rough fracture network

When fracturing reservoirs using supercritical $CO_2$, it is easier to activate natural fractures and form complex fracture networks compared to water-based fracturing fluids. The overall morphology of these fracture networks takes on an "X" or "Y" shape (Zhang et al., 2017), as shown in Fig. 1(a). Regardless of whether the fractures form an "X" or "Y" shape, their intersections are formed by the crossing of two perpendicular fractures. In this case, the shape of the entrance to the branching fractures is rectangular, thus classifying these types of fracture networks as X–Y patterns. Moreover, the fracture surfaces generated by supercritical $CO_2$ fracturing exhibit distinct curvatures and roughness, and the Synfrac open-source program can be used to obtain synthetic fractures that reflect real fracture morphologies (Ogilvie et al., 2006). By adjusting the spatial correlation of the fracture surface and the correlation between two surfaces, this program can mimic the surface and space characteristics of specific rock fractures. In our previous studies, we described in detail how to use the Synfrac program to generate rough synthetic fractures based on the morphological parameters of rock fractures induced by supercritical $CO_2$ fracturing (Zheng et al., 2023). The calculated range of the root mean square (RMS) value used to generate rough fractures ranged from 0.5 to 1.25 mm, while the fractal dimension varied between 2.1 and 2.4. Therefore, in this study we applied the same methodology to generate rough-walled fracture networks, where the fractal dimensions and RMS values of the various levels of fractures in the fracture network model were set to 2.3 and 0.75 mm, respectively, to match the characteristics of rough fracture surfaces produced by supercritical $CO_2$ fracturing.

Initially, independent primary fractures and branching fractures were created. Then, following the characteristic of intersecting fractures at different levels in the fracture network generated by supercritical $CO_2$ fracturing (X–Y pattern), the branching fractures were combined with the primary fractures to produce a simulated rough fracture network. In the rough fracture network model, the primary fractures (considered as hydraulic fractures) had a length of 200 mm, a height of 50 mm, and an average width of 2 mm. The secondary and tertiary fractures (considered as natural fractures) had a length of 100 mm, a height of 50 mm, and an average width of 1 mm. Within the fracture network, the secondary fractures intersected the primary fractures at a distance of 50 mm from the entrance, while the tertiary fractures intersected the secondary fractures at their centers. The angles between the fractures were all set at 60°. The resulting X–Y pattern rough fracture network model is shown in Fig. 1(b).

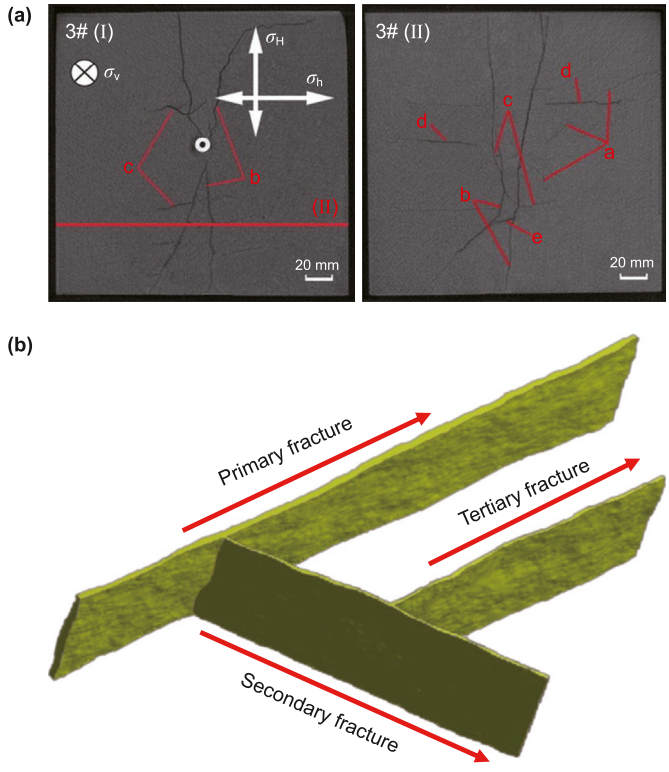


**Fig. 1.** Shape of fracture network in supercritical $CO_2$ fracturing: **(a)** "X" or "Y"-shape fracture networks resulting from supercritical $CO_2$ fracturing experiment (Zhang et al., 2017); **(b)** Schematic diagram of the complex fracture network of X–Y pattern with rough walls.

### 2.2. Mathematical model

The coupled computational fluid dynamics (CFD) and discrete element method (DEM) is a powerful tool for analyzing the particle behavior in fluid-particle two-phase flow (Norouzi et al., 2016). It allows for the retrieval of information for each individual particle, calculation of forces generated by contacts, evaluation of the particle's acceleration, velocity and displacement using Newton's second law, and provides a comprehensive understanding of the system's state. Additionally, it enables tracking of the motion trajectories of individual or groups of particles within the flow field. Thus, we utilized the CFD-DEM coupling method to develop a mathematical model that considers fluid flow and heat transfer within fractures to simulate the transport of proppants carried by supercritical $CO_2$. The mathematical model includes equations for mass, momentum, and energy transfer between particles and supercritical $CO_2$ fluid, as well as equations describing particle-particle and particle-wall collisions, which are detailed in our previous papers (Zheng et al., 2020, 2022a). In this study, we focus on presenting the model's assumptions and solution procedure.

In this study, we employed spherical proppant particles with identical diameters for the simulation, while neglecting heat transfer between fluid-particle, particle-particle, and particle-wall interactions. Heat transfer between fluid and walls was also taken into account. Additionally, due to the small scale of the fracture model, fluid leakage on the walls was disregarded in the simulation. Considering that the presence of proppant particles significantly influences the flow field, a bidirectional transient coupling approach was adopted in the model. At the end of each iteration in the computational fluid dynamics (CFD) simulation, the velocity, pressure, temperature, properties of supercritical $CO_2$, and the position information of particles were exchanged. Furthermore, as the time step for fluid computation was larger than that for particle computation in the DEM, the velocity, density, and pressure distribution of the fluid remained constant during each DEM step until the particle and fluid were synchronized in time, at which point the particle computation stopped and the fluid computation continued. The solution procedure of the model is illustrated in Fig. 2.

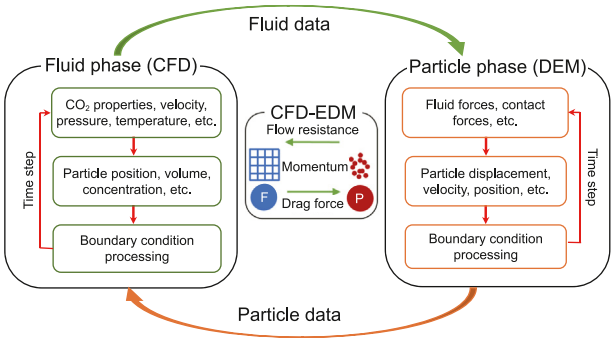


**Fig. 2.** Schematic of the model solution flow.

### 2.3. Model validation

In our previously published study, we compared the results obtained from this CFD-DEM model with experimental data of supercritical $CO_2$ transport proppant within a planar fracture (Zheng et al., 2023). It was found that the simulated dune morphology exhibited a favorable agreement with the experimental observations, with maximum errors of 4.43% and 5.56% observed for dune length and height, respectively, which indicated that the established mathematical model can well simulate the supercritical $CO_2$ transport proppant within the fracture. As for the accuracy of the proposed model in simulating the proppant turning transport behavior in the fracture network, the same was verified in another published study of ours (Zheng et al., 2020), which showed that the simulation results were closer to the morphology of the proppant dunes in the primary and branching fractures at different moments in the experimental data. Furthermore, the average error in the dimensionless height of the simulated proppant dunes, compared to the experimental measurements, was determined to be 2.16%. Considering the impact of certain mechanically estimated parameters on the simulation validation, the results from these two verifications collectively demonstrate the favorable reliability and computational precision of our developed CFD-DEM model in simulating the transport and placement of proppants carried by supercritical $CO_2$ within a network of fractures.

### 2.4. Boundary conditions

In the simulation, the boundary conditions were set as velocity inlet and pressure outlet, with the same pressure applied at the outlets of both the primary and branch fractures. No-slip boundary conditions were employed for the wall boundaries. During the fluid injection in reservoir stimulation, the temperature of the working fluid is typically lower than the reservoir temperature; therefore, the initial temperature of the injected fluid in this study was set lower than the wall temperature. The realizable $k-\varepsilon$ model was selected for calculating turbulence, and the phase coupled SIMPLE algorithm was employed to handle the coupling between pressure and momentum. The momentum, volume fraction, and energy equations were discretized using a first-order upwind scheme. The time step in the CFD simulations was set to $1 \times 10^{-4}$ s, while in the DEM simulations, it was set to $2 \times 10^{-6}$ s. Table 1 lists the detailed parameter settings used in the simulations, and the basis for these parameter settings can be derived from our previously published studies (Zheng et al., 2020, 2022b, 2023).

**Table 1**
Simulation parameter setting.

| Parameters | Values |
|---|---|
| Fractal dimension | 2.3 |
| RMS, mm | 0.75 |
| Proppant diameter, mm | 0.4 |
| Proppant density, kg/m$^3$ | 2650 |
| Slurry temperature, K | 338 |
| Wall temperature, K | 358 |
| Slurry injection velocity, m/s | 0.1, 0.2, 0.4 |
| Particle volumetric concentration, % | 1.5, 3, 6 |
| Outlet pressure, MPa | 18 |
| Particle Young's modulus, Pa | $5 \times 10^6$ |
| Particle Poisson's ratio | 0.5 |
| Wall Young's modulus, Pa | $3 \times 10^{10}$ |
| Wall Poisson's ratio | 0.3 |
| Restitution coefficient | 0.7 |
| Static friction coefficient | 0.5 |
| Rolling friction coefficient | 0.01 |

## 3. Results and analysis

### 3.1. Mechanisms of proppant turning transport within rough fracture network

Fig. 3 illustrates the overall distribution of proppant dunes formed by the transport of supercritical $CO_2$ slurry in both a smooth fracture network and a rough fracture network, as well as the morphology of proppant dunes deposited in the primary fractures and secondary fractures. The different colors of the proppant particles in the figure represent their respective velocities. In the simulations, the injection velocity of the slurry is set at 0.2 m/s, the diameter of the proppant is 0.4 mm, the density of the proppant is 2650 kg/m$^3$, and the proppant concentration is 3%. The boundary conditions used in the simulations for both fracture networks are identical. From Fig. 3, it can be observed that the distribution range of the proppant dunes in the two fracture networks is approximately the same, with none of the dunes entering the tertiary fractures. However, in terms of morphology, there are differences in the distribution patterns of dunes between the smooth fracture network (see Fig. 3(a)) and the rough fracture network (see Fig. 3(b)), particularly within the secondary fractures. This indicates that the transport characteristics of proppant entering the branch fractures in the rough fracture network may differ from those in the smooth fracture network.

Fig. 4 illustrates the transport characteristics of proppant transport from the primary fracture to the secondary fracture in both smooth and rough fracture networks, with the color of the proppant particles indicating their velocities. In the smooth fracture network, as shown in Fig. 4(a), at $t = 3$ s, the proppant particles entering the secondary fractures move downward along the surface of the dune from the primary fracture, exhibiting relatively low velocities. This indicates that the proppant particles in this case slide down the accumulated dune in the primary fractures under the influence of gravity, entering the secondary fracture. At $t = 9$ s, some proppant particles are suspended and carried into the secondary fractures by the fluid. This is due to the increased height of the dune in the primary fracture, which reduces the flow area within the fracture, increases the flow velocity in the upper part of the dune, and enhances the carrying capacity of the fluid. Consequently, proppant particles enter the secondary fractures through a combination of gravity-driven sliding and high velocity fluid suspension. When $t = 12$ s, it can be observed that the maximum

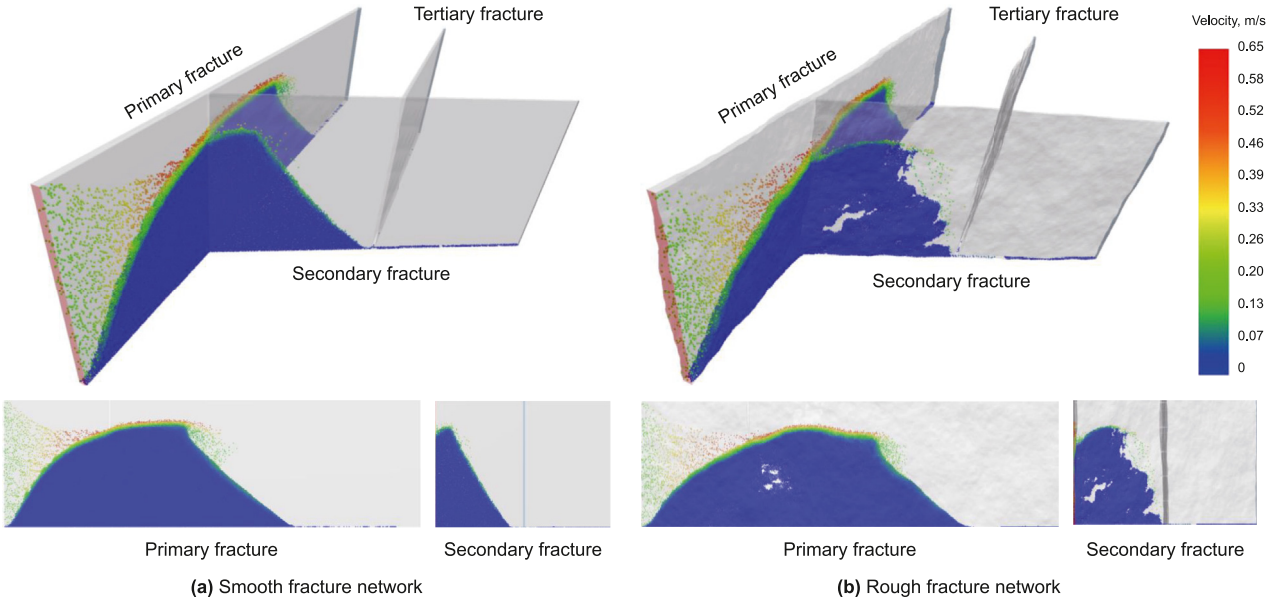


**(a)** Smooth fracture network **(b)** Rough fracture network

**Fig. 3.** Distribution of dune within different fracture networks.

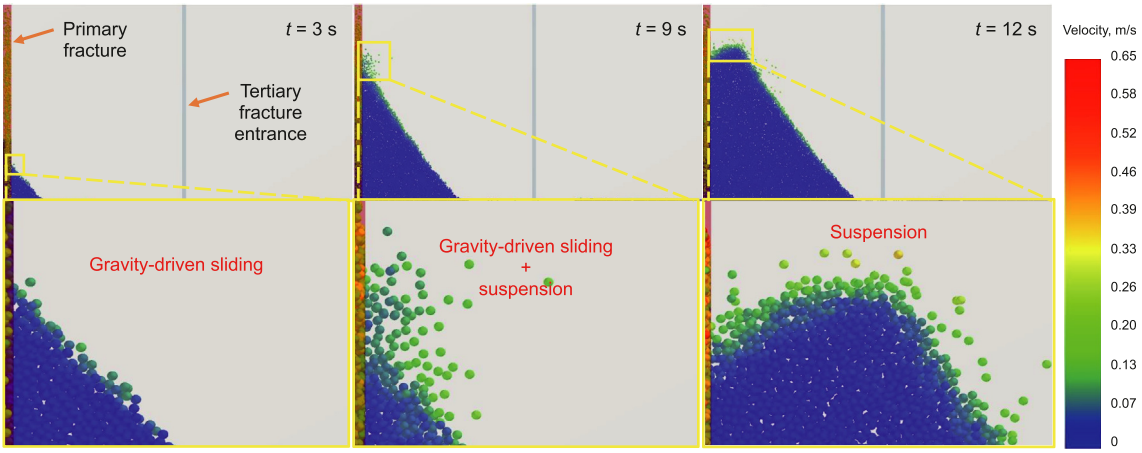


**(a)** Smooth fracture network

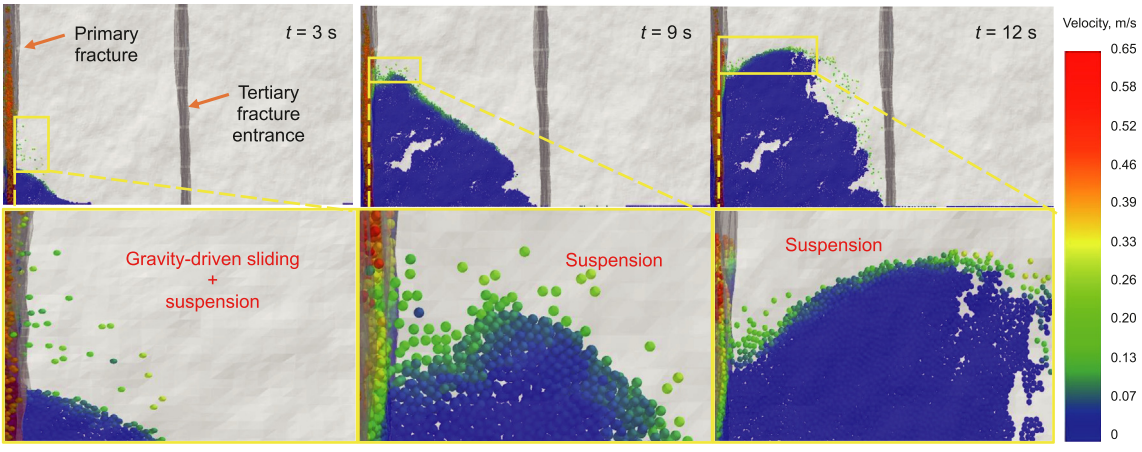


**(b)** Rough fracture network

**Fig. 4.** Characteristics of proppant turning transport in different fracture networks.

height of the dune within the secondary fractures exceeds that at the entrance, indicating that all proppant particles primarily enter the secondary fractures through suspension by the high-velocity fluid. Thus, in the smooth fracture network, the turning transport mechanism of proppant into the secondary fracture are gravity-driven sliding and high velocity fluid suspension, and the proppant particles mainly rely on high-velocity fluid suspension to enter the secondary fracture after the dune in the primary fracture reaches a certain height, which is in line with the phenomenon observed by Sahai et al. (2014) in their experimental study on proppant transport in smooth fracture networks.

The transport of proppant in a rough fracture network can be observed in Fig. 4(b). At $t = 3$ s, the proppant enters the secondary fractures through both gravity-driven sliding and suspension. At $t = 9$ s and $t = 12$ s, the maximum height of the dune within the secondary fractures exceeds that at the entrance, indicating that proppant primarily enters the secondary fractures through suspension, similar to the behavior seen in the smooth fracture network. It is worth noting that the particles in the rough fracture network are able to enter the secondary fracture in suspension at the initial stage of slurry injection at $t = 3$ s, i.e., when the flow channel area has not yet been significantly reduced by the influence of the dune buildup and the fluid flow velocity is low, which is significantly different from the proppant transport in the smooth fracture network, suggesting that the turning transport of the proppant in the rough fracture network is not only related to the fluid velocity in the primary fracture, but also to the fracture.

A comparison of the fluid Reynolds number near the entrance of the secondary fracture in the smooth fracture network and the rough fracture network at different moments is given in Fig. 5. It can be seen that the fluid Reynolds numbers near the entrance of the secondary fracture are closer in both fracture networks at $t = 3$ s. From the previous analysis, we already know that the proppant in the rough fracture network, however, is more likely to enter the secondary fracture in the form of suspension, and Fig. 5 shows that the hydraulic factor in the primary fracture is not the reason for the difference in the form of proppant transport in the two fracture networks as it turns to enter the branch fracture.

Fluid flow in a fracture is closely related to the shape of the flow channel (Zhang and Chai, 2020). The flow channel shapes localized in the primary fracture near the entrance of the secondary fracture

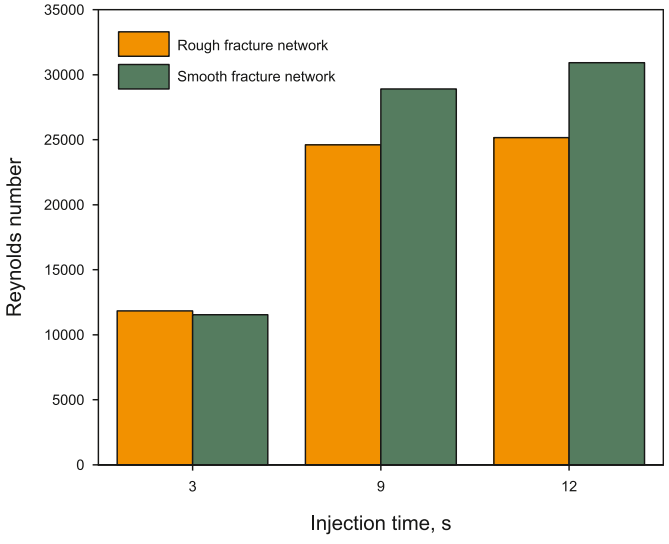


**Fig. 5.** Comparison of Reynolds number at the entrance of secondary fracture with different fracture networks.

in the rough and smooth fracture networks are given in Fig. 6, and the selected observation location is located at 5 mm from the entrance of the secondary fracture at the location of the red cross-section shown in Fig. 6(a). Fig. 6(b) and (c) show the observed channel shapes and proppant particle motion characteristics along the slurry flow direction ($X$-axis direction) at the selected locations in the rough and smooth fracture networks at $t = 3$ s, respectively.

From Fig. 6(b), it can be seen that the fluctuating walls in the rough fracture network make the spatial morphology of the flow channel inside the fracture complicated, and the curved flow channel increases the degree of tortuosity of the fluid flow path, which makes the flow direction and flow velocity changeable. The effect on the proppant transport is reflected in the different colors of particles suspended at different locations in the figure, i.e., the proppant particle velocity varies greatly. In Fig. 6(c), the smooth fracture network shows that the regular flow path makes the proppant particles uniform in color, and due to the influence of hydrodynamics, the particles tend to gather in the middle of the flow path when they are transported. On the other hand, it can also be observed from Fig. 6(b) that the boundary of the secondary fracture entrance in the rough fracture network is similarly meandering and undulating, and there is a partial protrusion of one side wall of the branch fracture into the flow channel of the primary fracture as shown by the dashed line part in the figure. This protrusion also induces the proppant particles suspended within the primary fracture to turn into the branch fracture as they flow through the branch fracture entrance.

A comparative analysis of the proppant particle transport characteristics in the two fracture networks shows that the irregular flow channel shape in the primary fracture of the rough fracture network results in variable fluid flow direction, which enhances the lateral movement of the particles, and thus increases the probability of the proppant flowing through the fracture intersections to enter the secondary fracture. At the same time, the meandering and irregular entrance interfaces of the branch fracture in the rough fracture network, and the induction of the fracture surface structure that protrudes into the flow channel of the primary fracture may also enable the suspended proppant to be turned to enter the branch fracture when the fluid flow velocity in the primary fracture is relatively low at the beginning of the injection period. In summary, the turning transport mechanisms of proppant into branch fractures in rough fracture networks are gravity-driven sliding, high velocity fluid suspension, and fracture structure induction.

### 3.2. Comparison of different fracturing fluids

This subsection compares the placement effects of water and supercritical $CO_2$ carrying proppant transport within a rough fracture network. In the simulations, the injection parameters were set the same in both cases except for the change in fluid type, with a slurry injection velocity of 0.2 m/s, a proppant size of 0.4 mm, a proppant density of 2650 kg/m$^3$, and a proppant concentration of 3%, outlet pressure 18 MPa.

Fig. 7 shows the placement of proppant dunes by water and supercritical $CO_2$ at different moments in all levels of the rough fracture network. It can be seen that using water to transport the proppant obtains a long spreading distance in all levels of fractures, and the proppant remains well suspended after entering the branch fractures and then settles at the bottom of the fractures. In supercritical $CO_2$ fluids, the proppant soon settles down and accumulates to form proppant dunes after entering the secondary fractures, and the placement effect in the tertiary fractures is significantly weaker than that of water.

Fig. 8 shows the changes of the average Reynolds number and

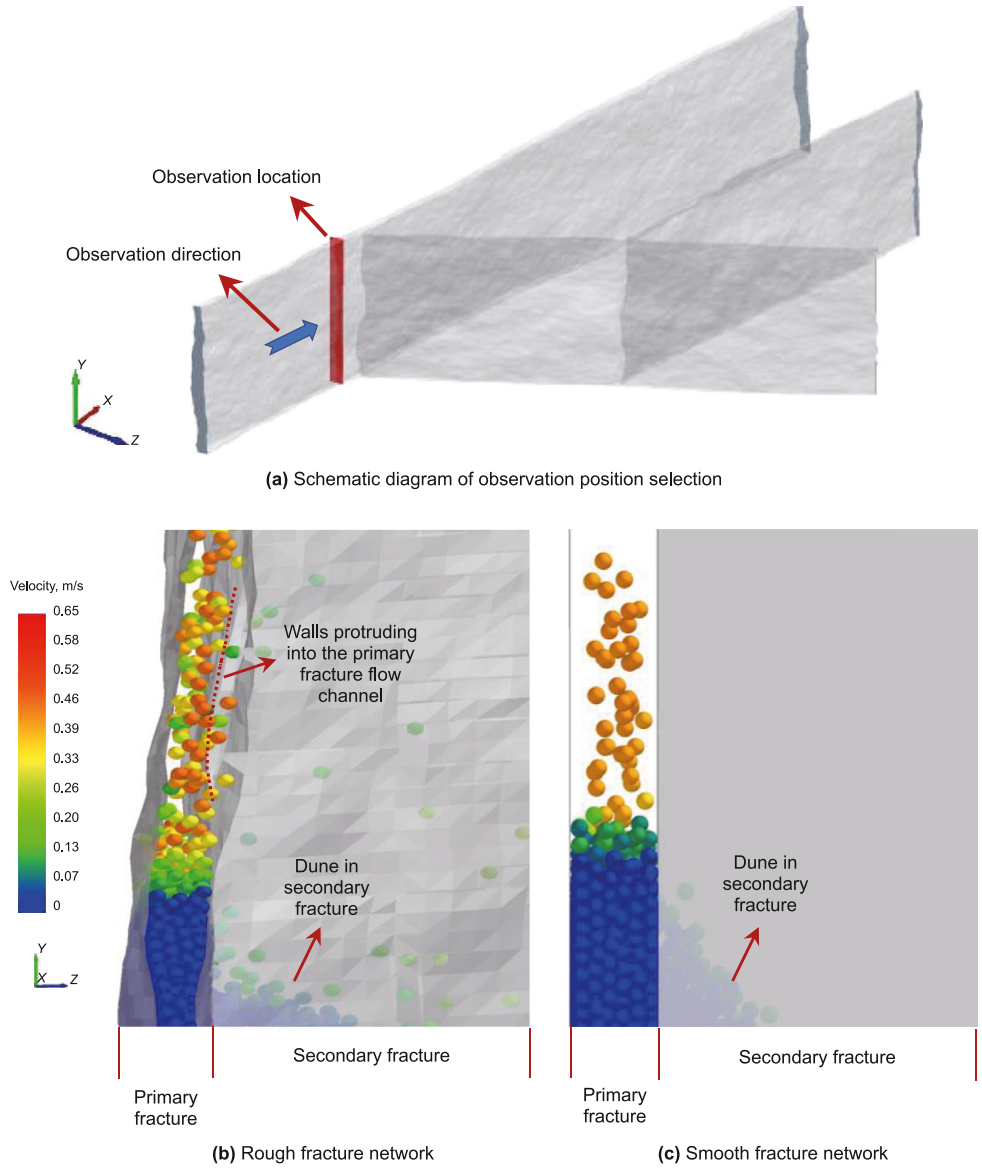


**(a)** Schematic diagram of observation position selection

**(b)** Rough fracture network

**(c)** Smooth fracture network

**Fig. 6.** Comparison of flow channel shape characteristics at the entrance of branch fractures in the two fracture networks.

the average fluid velocity of the fluid near the entrance of the secondary fracture in the primary fracture with time. It can be seen that the average flow velocity of supercritical $CO_2$ and water are closer at the initial moment, while both flow velocities increase with the increase of injection time, but the growth rate of supercritical $CO_2$ is larger than that of water. This is due to the fact that the proppant particles in the supercritical $CO_2$ slurry settle more easily and the proppant dunes accumulate faster, which in turn reduces the flow area of the fluid. In addition, it can also be seen from Fig. 8 that the Reynolds number near the entrance of the secondary fracture is significantly larger than that of the water when supercritical $CO_2$ delivers the proppant, which is mainly due to the low viscosity of supercritical $CO_2$.

From the above analysis, it can be seen that when supercritical $CO_2$ slurry flows in the rough fracture network, although the proppant can enter the secondary fracture in the form of suspension due to the induced fracture structure and fluid turbulence, it still settles and accumulates in the branching fracture very quickly. In contrast, water is able to carry the proppant in suspension into the secondary fracture for a longer distance than supercritical $CO_2$ with the same fracture structure and smaller average fluid velocity and Reynolds number near the entrance of the secondary fracture, indicating that the fluid viscosity affects proppant transport more than the high Reynolds number of the fluid.

### 3.3. *Influence of supercritical $CO_2$ viscosity*

The lower viscosity of supercritical $CO_2$ makes it disadvantageous in carrying proppant transportation, and viscosity enhancement of the fluid is a potential way to solve this problem. Since the viscosity of supercritical $CO_2$ changes with temperature as it flows through a fracture, this subsection builds on the case in Section 3.1 by multiplying the viscosity formula by 10, 20, and 40, respectively, and thus obtaining supercritical $CO_2$ fluids with different viscosity multipliers increased, expressed as 10, 20, and 40 times. Fig. 9 demonstrates the distribution of proppant within each level of fracture in the rough fracture network for different fluid viscosities. The injection velocity of supercritical $CO_2$ slurry in the simulation is

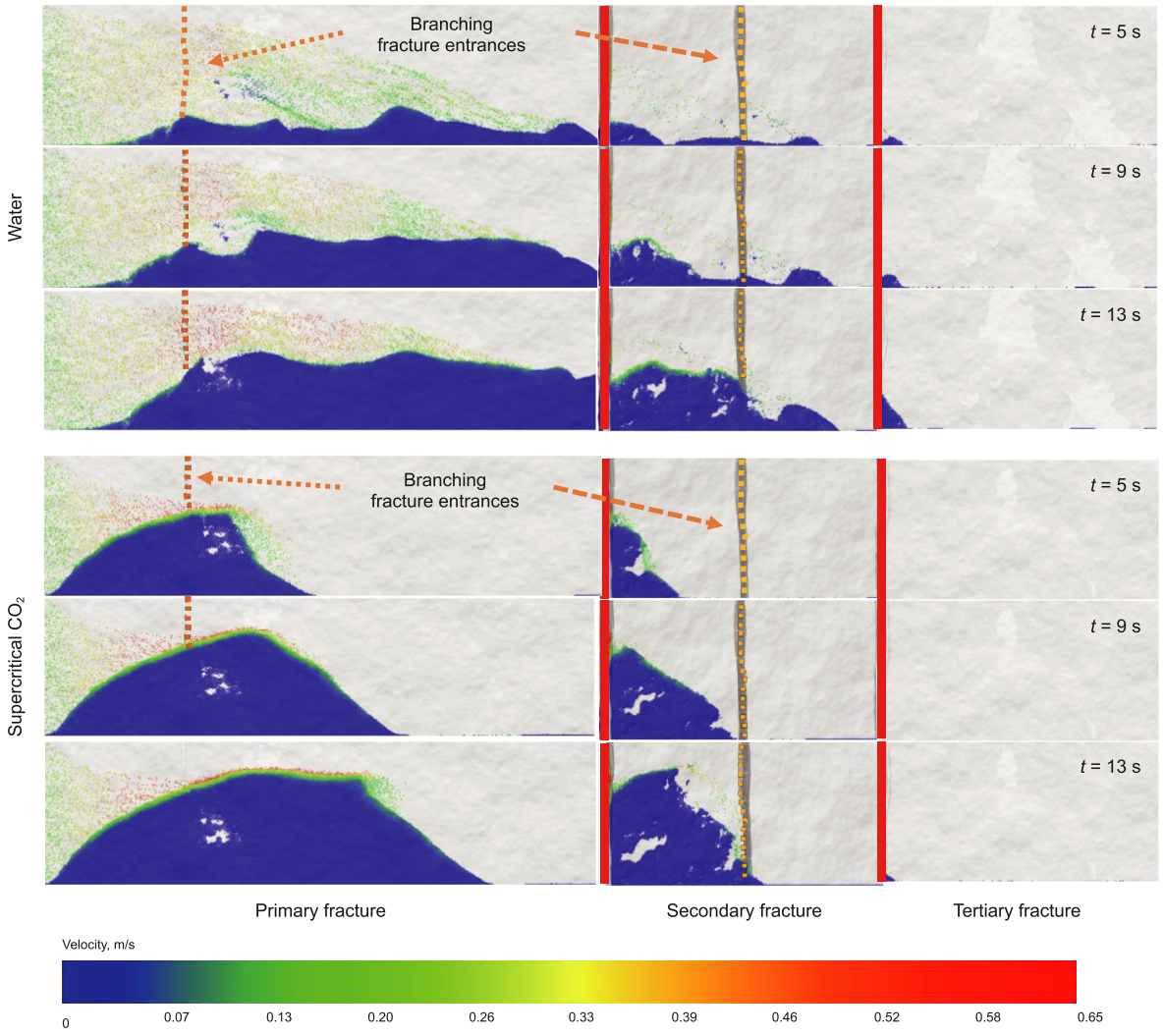


**Fig. 7.** Comparison of the ability of different fluids to carry proppant.

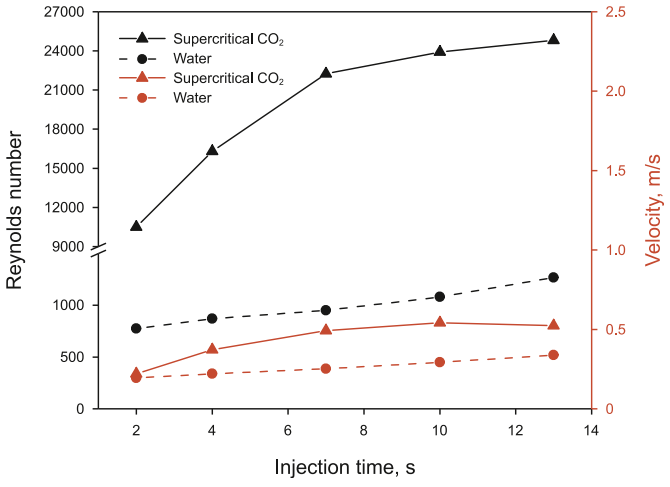


**Fig. 8.** Reynolds number and velocity variation of different fluids near the entrance of the secondary fracture.

0.2 m/s, the proppant size is 0.4 mm, the proppant density is 2650 kg/m$^3$, and the proppant concentration is 3%. From the figure, it can be seen that after increasing the viscosity of supercritical $CO_2$ by 10 and 20 times, respectively, the proppant placement in the branch fractures, especially in the tertiary fractures, was not significantly improved. However, when the viscosity was increased by 40 times, the settlement buildup of the proppant during transportation within the fracture was significantly weakened, and the transportation distance within the branching fracture was significantly improved. This suggests that viscosity increase for supercritical $CO_2$ needs to reach a certain value to significantly improve its proppant-carrying effect.

Fig. 10 gives the variation of the amount of proppant entering inside the branching fracture as a percentage of the total amount injected with time after increasing the viscosity of supercritical $CO_2$ by different multiples. From the figure, it can be seen that the percentage of proppant particles entering inside the branching fracture increases as the viscosity multiplier increases, which is due to the fact that the increase in fluid viscosity improves the carrying capacity of the particles, allowing them to follow the fluid into the branching fracture. In addition, it is possible to note that the difference in the percentage of particles entering the branching fracture between 20 times and 40 times increase in fluid viscosity is not significant, and this is because the location of the branching fracture from the inlet affects the amount of proppant that enters it.

Usually, due to the limitation of the fracturing fluid's carrying

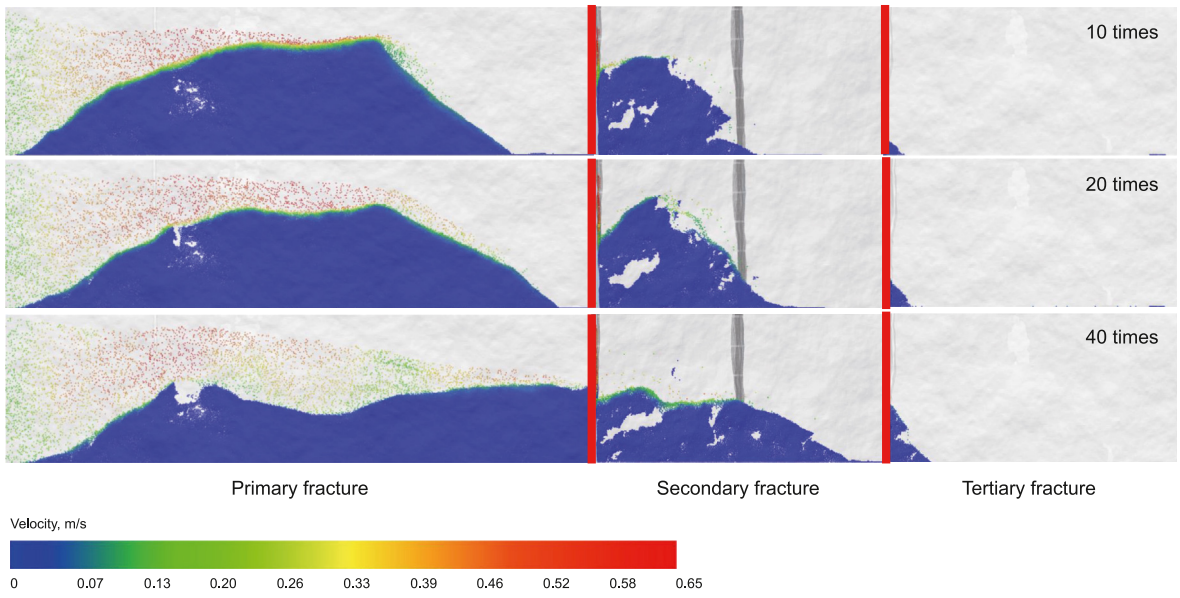


**Fig. 9.** Distribution of dunes in the rough fracture network with different fluid viscosities.

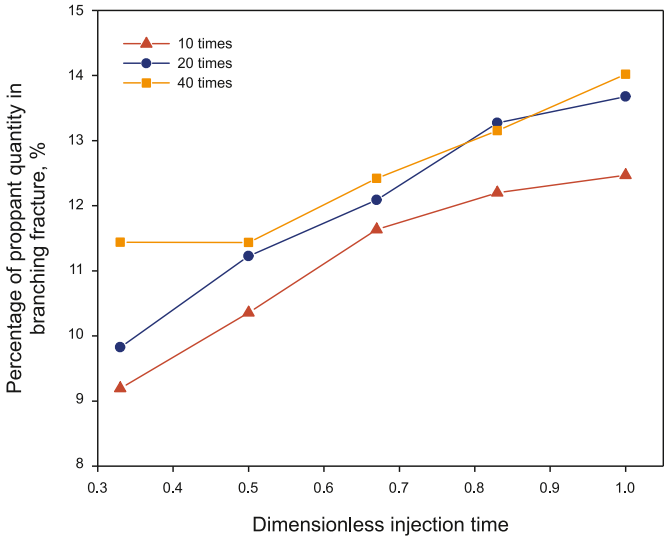


**Fig. 10.** Percentage of proppant particles in branch fractures with different fluid viscosities.

capacity, the proppant is not completely suspended in the fluid, but gradually settles with the increase of the flow distance, so the further the branch fracture is from the inlet, the lower the amount of proppant flowing into it. In the fracture model used in this simulation, the branch fracture is closer to the entrance of the primary fracture, and it can be seen in Fig. 9 that the height of the proppant dunes accumulated near the intersection of the branch fracture is similar between 20 times and 40 times increase in viscosity, which means that the difference between the two in terms of the carrying capacity is not obvious at this distance, and therefore the number of particles entering the branch fracture is closer. However, we can see from the placement distance of the proppant dunes within the branch fractures that the supercritical $CO_2$ slurry with 40 times increase in fluid viscosity is more advantageous in supporting the branching fractures. In summary, the supercritical $CO_2$ viscosity increase needs to be more than 20 times (about 0.94 mPa s) under the simulation conditions in this paper to produce a significant improvement in its proppant-carrying effect.

### 3.4. Influence of injection velocity

Fig. 11 illustrates the distribution of proppant within each level of the rough fracture network for different slurry injection velocities (0.1, 0.2 and 0.4 m/s). The proppant size in the simulation is 0.4 mm, the proppant density is 2650 kg/m$^3$, and the proppant concentration is 3%. From the figure, it can be seen that the proppant is difficult to be transported to the tertiary fracture at low injection rate, and with the increase of supercritical $CO_2$ slurry injection velocity, the transportation distance of proppant inside the fracture at all levels is significantly increased, and more particles enter the tertiary fracture. By comparing the difference in the height of the proppant dunes at the entrance of the secondary fracture and the maximum height of the proppant dunes within the secondary fracture, it was found that the height of the proppant dunes within the secondary fracture was greater than the height of its entrance, which indicated that the proppant entered the secondary fracture more in the form of suspension at the high injection velocity. In addition, when the injection velocity was 0.4 m/s, the formation of proppant sprinkle due to bridging within the primary fracture, superimposed on the higher initial injection velocity, resulted in a significant increase in the laying distance of the proppant dune within the primary fracture.

Fig. 12 compares the variation of the percentage of proppant quantity within the branch fractures (secondary versus tertiary fractures) to the total injected quantity with time for different injection velocities. From the figure, it can be seen that the percentage of the proppant quantity inside the branch fractures tends to increase with the increase of the injection time, and at the same time, increasing the injection velocity makes the percentage of the proppant quantity inside the branch fractures increase significantly, which means that more proppant enters into the branch fractures. Therefore, increasing the injection velocity can significantly improve the propping effect on branch fractures.

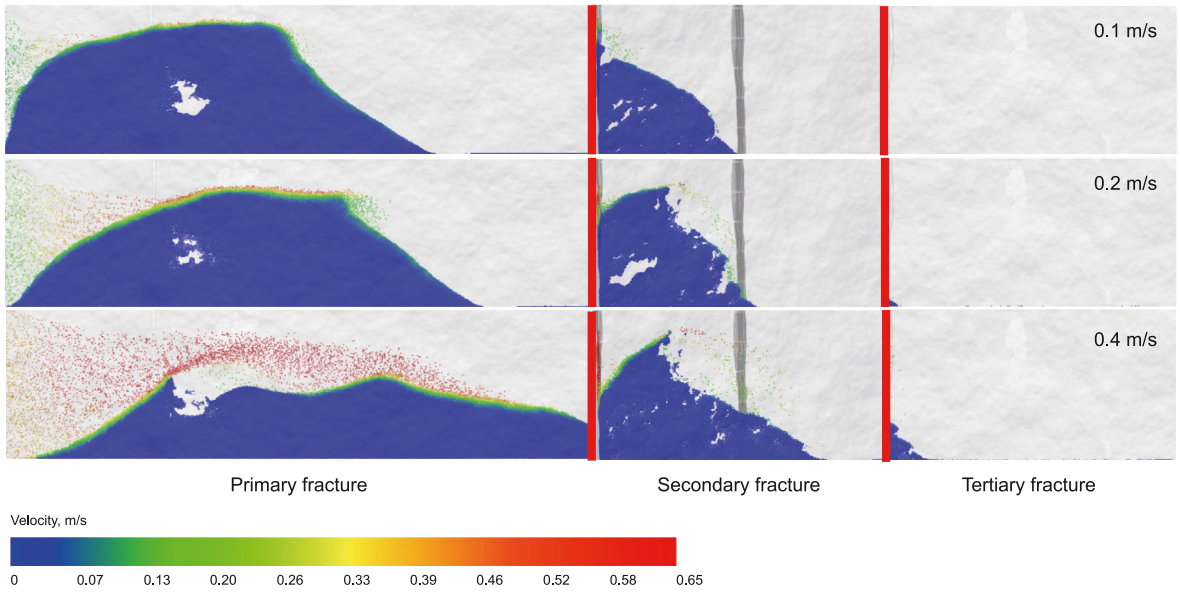


**Fig. 11.** Distribution of dunes in the rough fracture network with different injection velocities.

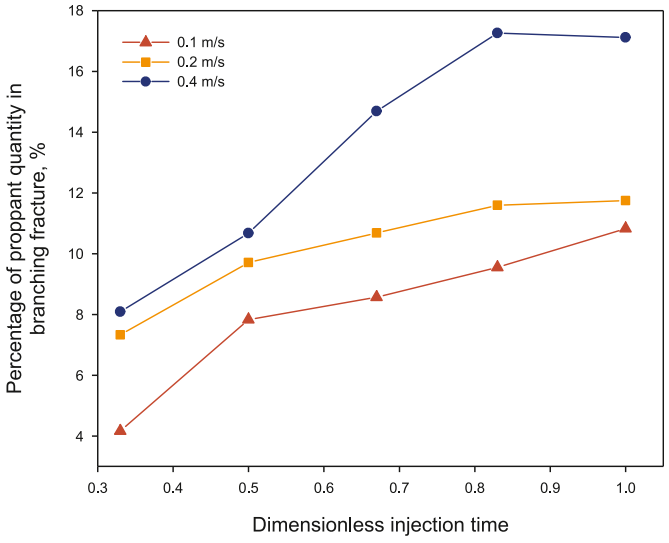


**Fig. 12.** Percentage of proppant particles in branch fractures with different injection velocities.

### 3.5. *Influence of proppant concentration*

Fig. 13 illustrates the distribution of proppant within each level of fracture in the rough fracture network for different proppant concentrations (1.5%, 3% and 6%). The injection rate of proppant slurry in the simulation is 0.2 m/s, the proppant size is 0.4 mm, and the proppant density is 2650 kg/m$^3$. When the proppant concentration was increased from 1.5% to 3%, the proppant transport distance within the primary fracture changed from 168.9 to 163.6 mm, which was 3.14% shorter. The distance within the secondary fracture changed from 62.59 to 54.34 mm, which was 13.18% shorter, and the amount of proppant entering the tertiary fracture decreased significantly. It can be seen in Fig. 13 that when the proppant concentration was increased to 6%, proppant transport was impeded by a partial bridging at the entrance of the secondary fracture, and the height of the proppant dune within the secondary fracture was significantly lower than that within the primary fracture. Proppant transport in smooth fracture networks is thought to be unaffected by fracture complexity within secondary and tertiary fractures as long as a sufficient amount of proppant is injected, and the amount of proppant within a branching fracture is dependent on the height of the proppant dune within the previous fracture, and increasing the proppant concentration enhances proppant transport (Alotaibi and Miskimins, 2018). Whereas, as can be seen in Fig. 13, the effect of potential bridging blockage on proppant entry into branching fractures due to the irregular shape of branching fracture entrances in a rough fracture network suggests that such proppant pumping strategies as those described above in smooth fracture networks are not fully applicable in practice.

Fig. 14 shows the variation of the percentage of the amount of proppant in the branch fracture to the total injected amount with time for different proppant concentrations, and it can be seen that the percentage of proppant entering the branch fracture does not always increase with the increase of the injection time. When the proppant concentration was 6%, the percentage of proppant inside the branch fracture first increased and then decreased, which can be seen from the above analysis that this is due to the local bridging at the entrance of the secondary fracture, which significantly reduces the efficiency of proppant placement inside the secondary fracture. In contrast, the percentage within the branch fractures increased again in the later stages of injection when the height of the proppant dune within the primary fracture exceeded the bridging point. Overall, the change of proppant concentration has a significant effect on the percentage of proppant within the branch fractures, and the lower concentration helps to weaken the potential bridging occurrence of proppant at the fracture intersection, and at the same time favors to obtain a longer transport distance to enhance the filling effect of supercritical $CO_2$ proppant slurry on the branch fractures. Under the simulation conditions in this paper, a proppant concentration of no more than 3% yields a more desirable proppant placement.

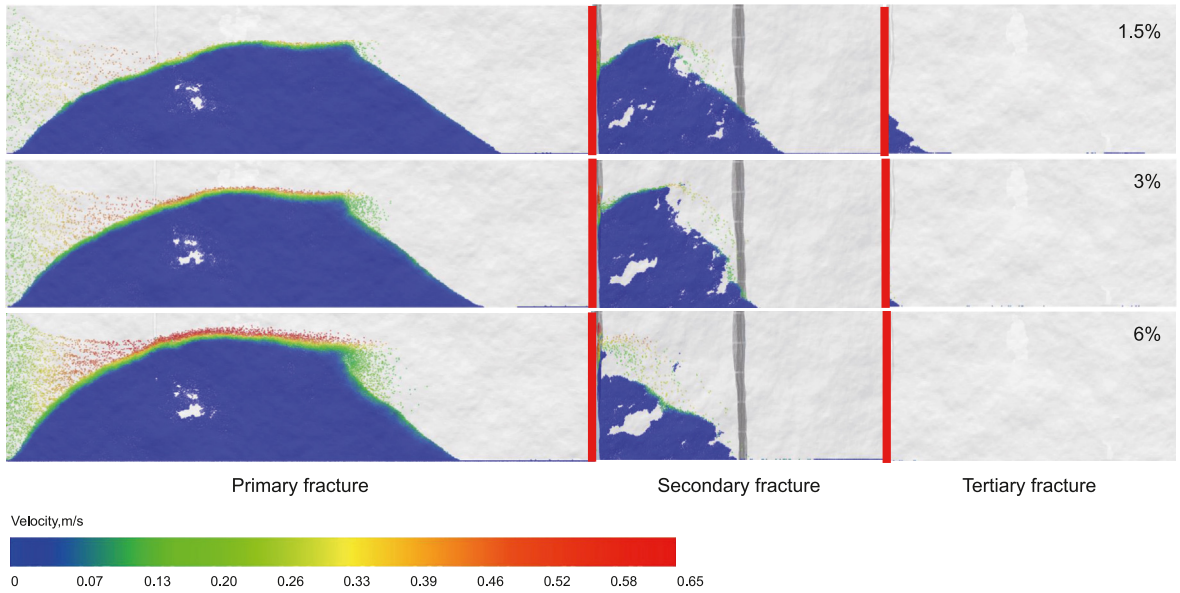


**Fig. 13.** Distribution of dunes in the rough fracture network with different proppant concentrations.

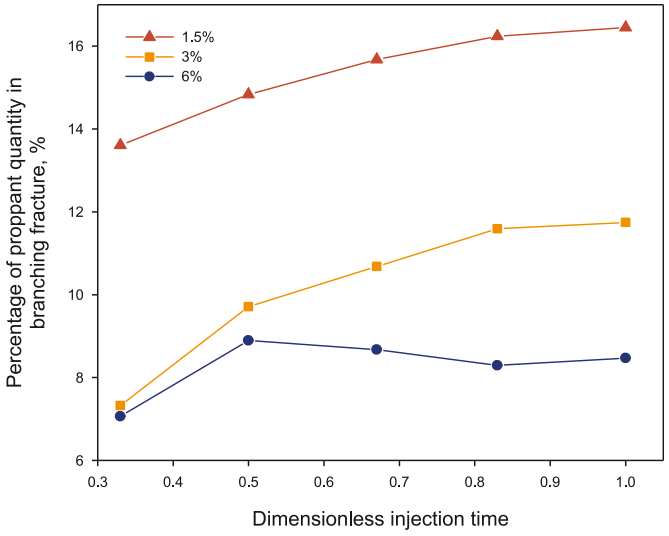


**Fig. 14.** Percentage of proppant particles in branch fractures with different proppant concentrations.

## 4. Conclusions

In this paper, a fracture network model with rough walls is constructed based on the characteristics of the fracture network formed by supercritical $CO_2$ fracturing, and the reliability of the established CFD-DEM model in simulating the proppant turning transport in complex fracture networks is demonstrated. By comparing with the proppant transport behavior within the smooth fracture network, the turning transport mechanism of the proppant into the branch fracture in the rough fracture network is revealed, and the influence of key pumping parameters on the proppant into the branch fracture is analyzed. Under the research conditions of this paper, the following conclusions are obtained.

(1) The tortuous fracture surface morphology in the rough fracture network leads to irregular variation in the flow channel shape and branch fracture entrance interface, resulting in a different mechanism for proppant turning and transport in the rough fracture network than in the smooth fracture network.

(2) When proppant is transported through a network of rough fractures formed by hydraulic fracturing, the turning transport mechanisms into branching fractures are gravity-driven sliding, high velocity fluid suspension, and fracture structure induction, where fracture structure induction is not present in smooth fracture networks.

(3) Under the same injection conditions, supercritical $CO_2$ with high flow Reynolds number is still weaker than water in its ability to transport proppant into the secondary fracture, indicating that fluid viscosity affects proppant transport to a greater extent than high fluid Reynolds number at this point.

(4) Viscosity enhancement of supercritical $CO_2$ is a potential way to improve the ability of the fluid to carry the proppant, but the viscosity enhancement needs to exceed a certain value to have a significant effect, which is more than a factor of 20 (about 0.94 mPa s) under simulated conditions.

(5) Increasing the injection rate and decreasing the proppant concentration can enhance the proportion of proppant particles in the branch fractures, which is conducive to the support of the branch fractures, and then obtain a better reservoir stimulation effect.

## CRediT authorship contribution statement

**Yong Zheng:** Writing – original draft, Software, Methodology, Investigation, Formal analysis. **Meng-Meng Zhou:** Resources. **Ergun Kuru:** Writing – review & editing, Software. **Bin Wang:** Visualization, Validation. **Jun Ni:** Investigation, Funding acquisition. **Bing Yang:** Validation, Investigation. **Ke Hu:** Visualization, Investigation. **Hai Huang:** Validation, Resources, Funding acquisition.

**Hai-Zhu Wang:** Supervision, Funding acquisition, Conceptualization.

## Declaration of competing interest

The authors declared that they have no conflicts of interest to this work. We declare that we do not have any commercial or associative interest that represents a conflict of interest in connection with the work submitted.

## Acknowledgments

The authors would like to acknowledge the support from the National Key Research and Development Program of China (Grant No. 2022YFE0137200), the Natural Science Basic Research Program of Shaanxi Province, China (Program No. 2024JC-YBQN-0381, 2023-JC-QN-0403), the Natural Science Basic Research Program of Shaanxi Province, China (Program No. 2022JC-37), the Innovation Capability Support Program of Shaanxi (Program No. 2023-CX-TD-31), the Funded by Open Foundation of Shaanxi Key Laboratory of Carbon Dioxide Sequestration and Enhanced Oil Recovery, and the Youth Innovation Team of Shaanxi Universities. The authors would also like to thank the editor and the anonymous reviewers for their constructive and valuable comments and suggestions.

## References

Ahamed, M., Perera, M., Elsworth, D., Ranjith, P., Matthai, S., Li, D., 2021. Effective application of proppants during the hydraulic fracturing of coal seam gas reservoirs: implications from laboratory testings of propped and unpropped coal fractures. Fuel 304, 121394. https://doi.org/10.1016/j.fuel.2021.121394.

Alotaibi, M.A., Miskimins, J.L., 2018. Slickwater proppant transport in hydraulic fractures: new experimental findings and scalable correlation. SPE Prod. Oper. 33 (2), 164–178. https://doi.org/10.2118/174828-MS.

Barboza, B.R., Chen, B., Li, C., 2021. A review on proppant transport modelling. J. Petrol. Sci. Eng. 204, 108753. https://doi.org/10.1016/j.petrol.2021.108753.

Cipolla, C.L., Warpinski, N.R., Mayerhofer, M.J., Lolon, E., Vincent, M.C., 2008. The relationship between fracture complexity, reservoir properties, and fracture treatment design. In: SPE Annual Technical Conference and Exhibition. https://doi.org/10.2118/115769-MS.

Coulter, G.R., Benton, E.G., Thomson, C.L., 2004. Water fracs and sand quantity: a Barnett shale example. In: SPE Annual Technical Conference and Exhibition. https://doi.org/10.2118/90891-MS.

Davoodi, S., Al-Shargabi, M., Wood, D.A., Rukavishnikov, V.S., 2023. A comprehensive review of beneficial applications of viscoelastic surfactants in wellbore hydraulic fracturing fluids. Fuel 338, 127228. https://doi.org/10.1016/j.fuel.2022.127228.

Dou, L., Li, D., Wen, Z., Wang, Z., Mi, S., Zhang, Q., 2022. History and outlook of global oil and gas resources evaluation. Acta Pet. Sin. 43 (8), 1035. https://doi.org/10.7623/syxb202208001.x (in Chinese).

Estrada, J.M., Bhamidimarri, R., 2016. A review of the issues and treatment options for wastewater from shale gas extraction by hydraulic fracturing. Fuel 182, 292–303. https://doi.org/10.1016/j.fuel.2016.05.051.

Haq, B., Muhammed, N.S., Liu, J., Chua, H.T., 2023. Enhanced natural gas production using $CO_2$ injection: application to sustainable hydrogen production. Fuel 347, 128474. https://doi.org/10.1016/j.fuel.2023.128474.

Hyman, J.D., Jimenez-Martinez, J., Viswanathan, H.S., et al., 2016. Understanding hydraulic fracturing: a multi-scale problem. Philos Trans A Math Phys Eng Sci 374 (2078). https://doi.org/10.1098/rsta.2015.0426.

Isah, A., Hiba, M., Al-Azani, K., Aljawad, M.S., Mahmoud, M., 2021. A comprehensive review of proppant transport in fractured reservoirs: experimental, numerical, and field aspects. J. Nat. Gas Sci. Eng. 88, 103832. https://doi.org/10.1016/j.jngse.2021.103832.

Jackson, R.B., Vengosh, A., Carey, J.W., Davies, R.J., Darrah, T.H., O'sullivan, F., Pétron, G., 2014. The environmental costs and benefits of fracking. Annu. Rev. Environ. Resour. 39, 327–362. https://doi.org/10.1146/annurev-environ-031113-144051.

King, G.E., 2010. Thirty years of gas shale fracturing: what have we learned? In: SPE Annual Technical Conference and Exhibition. https://doi.org/10.2118/133456-MS.

Kou, R., Moridis, G., Blasingame, T., 2019. Bridging criteria and distribution correlation for proppant transport in primary and secondary fracture. In: SPE Hydraulic Fracturing Technology Conference and Exhibition. https://doi.org/10.2118/194319-MS.

Li, J., He, S., Wu, M., Liu, P., 2023. A comprehensive review of the proppant transportation in different simplified fracture models: experimentation, modeling, and prospects. Geoenergy Science and Engineering, 211974. https://doi.org/10.1016/j.geoen.2023.211974.

Liu, B., Yao, J., Sun, H., Zhang, L., 2024. Revealing the effects of thermal properties of supercritical $CO_2$ on proppant migration in supercritical $CO_2$ fracturing. Gas Science and Engineering 121, 205172. https://doi.org/10.1016/j.jgsce.2023.205172.

Middleton, R., Viswanathan, H., Currier, R., Gupta, R., 2014. $CO_2$ as a fracturing fluid: potential for commercial-scale shale gas production and $CO_2$ sequestration. Energy Proc. 63, 7780–7784. https://doi.org/10.1016/j.egypro.2014.11.812.

Middleton, R.S., Carey, J.W., Currier, R.P., et al., 2015. Shale gas and non-aqueous fracturing fluids: opportunities and challenges for supercritical $CO_2$. Appl. Energy 147, 500–509. https://doi.org/10.1016/j.apenergy.2015.03.023.

Middleton, R.S., Gupta, R., Hyman, J.D., Viswanathan, H.S., 2017. The shale gas revolution: barriers, sustainability, and emerging opportunities. Appl. Energy 199, 88–95. https://doi.org/10.1016/j.apenergy.2017.04.034.

Mojid, M.R., Negash, B.M., Abdulelah, H., Jufar, S.R., Adewumi, B.K., 2021. A state – of – art review on waterless gas shale fracturing technologies. J. Petrol. Sci. Eng. 196, 108048. https://doi.org/10.1016/j.petrol.2020.108048.

Norouzi, H.R., Zarghami, R., Sotudeh-Gharebagh, R., Mostoufi, N., 2016. Coupled CFD-DEM Modeling: Formulation, Implementation and Application to Multiphase Flows. Wiley Sons, West Sussex.

Ogilvie, S.R., Isakov, E., Glover, P.W., 2006. Fluid flow through rough fractures in rocks. II: a new matching model for rough rock fractures. Earth Planet Sci. Lett. 241 (3–4), 454–465. https://doi.org/10.1016/j.epsl.2005.11.041.

Roostaei, M., Nouri, A., Hosseini, S.A., et al., 2020. A concise review of experimental works on proppant transport and slurry flow. In: SPE International Conference and Exhibition on Formation Damage Control. https://doi.org/10.2118/199310-MS.

Sahai, R., Miskimins, J.L., Olson, K.E., 2014. Laboratory results of proppant transport in complex fracture systems. In: SPE Hydraulic Fracturing Technology Conference. https://doi.org/10.2118/168579-MS.

Sahai, R., Moghanloo, R.G., 2019. Proppant transport in complex fracture networks—a review. J. Petrol. Sci. Eng. 182, 106199. https://doi.org/10.1016/j.petrol.2019.106199.

Song, X., Guo, Y., Zhang, J., et al., 2019. Fracturing with carbon dioxide: from microscopic mechanism to reservoir application. Joule 3 (8), 1913–1926. https://doi.org/10.1016/j.joule.2019.05.004.

Sun, B., Wang, J., Wang, Z., Gao, Y., Xu, J., 2018. Calculation of proppant-carrying flow in supercritical carbon dioxide fracturing fluid. J. Petrol. Sci. Eng. 166, 420–432. https://doi.org/10.1016/j.petrol.2018.03.051.

Tong, S., Mohanty, K.K., 2016. Proppant transport study in fractures with intersections. Fuel 181, 463–477. https://doi.org/10.1016/j.fuel.2016.04.144.

Vengosh, A., Jackson, R.B., Warner, N., Darrah, T.H., Kondash, A., 2014. A critical review of the risks to water resources from unconventional shale gas development and hydraulic fracturing in the United States. Environ. Sci. Technol. 48 (15), 8334–8348. https://doi.org/10.1021/es405118y.

Vidic, R.D., Brantley, S.L., Vandenbossche, J.M., Yoxtheimer, D., Abad, J.D., 2013. Impact of shale gas development on regional water quality. Science 340 (6134), 1235009. https://doi.org/10.1126/science.1235009.

Wang, H., Wang, M., Yang, B., Lu, Q., Zheng, Y., Zhao, H., 2018a. Numerical study of supercritical $CO_2$ and proppant transport in different geometrical fractures. Greenhouse Gases-Science and Technology 8 (5), 898–910. https://doi.org/10.1002/ghg.1803.

Wang, J., 2020. Continuum theory for dense gas-solid flow: a state-of-the-art review. Chem. Eng. Sci. 215, 115428. https://doi.org/10.1016/j.ces.2019.115428.

Wang, J., Elsworth, D., Wu, Y., Liu, J., Zhu, W., Liu, Y., 2018b. The influence of fracturing fluids on fracturing processes: a comparison between water, oil and SC-$CO_2$. Rock Mech. Rock Eng. 51, 299–313. https://doi.org/10.1007/s00603-017-1326-8.

Wang, T., Zhang, F., Furtney, J., Damjanac, B., 2022. A review of methods, applications and limitations for incorporating fluid flow in the discrete element method. J. Rock Mech. Geotech. Eng. 14 (3), 1005–1024. https://doi.org/10.1016/j.jrmge.2021.10.015.

Wang, X., Gong, L., Li, Y., Yao, J., 2023. Developments and applications of the CFD-DEM method in particle–fluid numerical simulation in petroleum engineering: a review. Appl. Therm. Eng. 222, 119865. https://doi.org/10.1016/j.applthermaleng.2022.119865.

Yang, B., Wang, H.-Z., Li, G.-S., et al., 2022. Fundamental study and utilization on supercritical $CO_2$ fracturing developing unconventional resources: current status, challenge and future perspectives. Petrol. Sci. 19 (6), 2757–2780. https://doi.org/10.1016/j.petsci.2022.08.029.

Yao, S., Chang, C., Hai, K., Huang, H., Li, H., 2022. A review of experimental studies on the proppant settling in hydraulic fractures. J. Petrol. Sci. Eng. 208, 109211. https://doi.org/10.1016/j.petrol.2021.109211.

Yuan, B., Wood, D.A., 2018. A holistic review of geosystem damage during unconventional oil, gas and geothermal energy recovery. Fuel 227, 99–110. https://doi.org/10.1016/j.fuel.2018.04.082.

Zeng, J., Li, H., Zhang, D., 2019. Numerical simulation of proppant transport in propagating fractures with the multi-phase particle-in-cell method. Fuel 245, 316–335. https://doi.org/10.1016/j.fuel.2019.02.056.

Zhang, B., Zhang, C., Ma, Z., Zhou, J., Liu, X., Zhang, D., Ranjith, P., 2023. Simulation study of micro-proppant carrying capacity of supercritical $CO_2$ (Sc-$CO_2$) in secondary fractures of shale gas reservoirs. Geoenergy Science and Engineering 224, 211636. https://doi.org/10.1016/j.geoen.2023.211636.

Zhang, C., Liu, S., Ma, Z., Ranjith, P., 2021a. Combined micro-proppant and

supercritical carbon dioxide (SC-$CO_2$) fracturing in shale gas reservoirs: a review. Fuel 305, 121431. https://doi.org/10.1016/j.fuel.2021.121431.
Zhang, D., Yang, T., 2015. Environmental impacts of hydraulic fracturing in shale gas development in the United States. Petrol. Explor. Dev. 42 (6), 876–883. https://doi.org/10.1016/S1876-3804(15)30085-9.
Zhang, X., Lu, Y., Tang, J., Zhou, Z., Liao, Y., 2017. Experimental study on fracture initiation and propagation in shale using supercritical carbon dioxide fracturing. Fuel 190, 370–378. https://doi.org/10.1016/j.fuel.2016.10.120.
Zhang, X., Wei, B., You, J., Liu, J., Wang, D., Lu, J., Tong, J., 2021b. Characterizing pore-level oil mobilization processes in unconventional reservoirs assisted by state-of-the-art nuclear magnetic resonance technique. Energy 236, 121549. https://doi.org/10.1016/j.energy.2021.121549.
Zhang, Y., Chai, J., 2020. Effect of surface morphology on fluid flow in rough fractures: a review. J. Nat. Gas Sci. Eng. 79, 103343. https://doi.org/10.1016/j.jngse.2020.103343.
Zheng, Y., Wang, H., Li, G., Tian, G., Yang, B., Liu, M., 2022a. Proppant transport characteristics in tortuous fractures induced by supercritical $CO_2$ fracturing. Nat. Gas. Ind. B 9 (5), 457–466. https://doi.org/10.1016/j.ngib.2022.03.005.
Zheng, Y., Wang, H., Li, Y., Tian, G., Yang, B., Zhao, C., Liu, M., 2021. Effect of proppant pumping schedule on the proppant placement for supercritical $CO_2$ fracturing. Petrol. Sci. https://doi.org/10.1016/j.petsci.2021.11.002.
Zheng, Y., Wang, H., Tian, G., Liu, M., Li, G., Kuru, E., 2022b. Experimental investigation of proppant transport in hydraulically fractured wells using supercritical $CO_2$. J. Petrol. Sci. Eng. 110907. https://doi.org/10.1016/j.petrol.2022.110907.
Zheng, Y., Wang, H., Wang, B., et al., 2023. Effect of roughness characteristics of hydraulic fractures on the proppant transport using supercritical $CO_2$. Geoenergy Science and Engineering 227, 211908. https://doi.org/10.1016/j.geoen.2023.211908.
Zheng, Y., Wang, H., Yang, B., Hu, Y., Shen, Z., Wen, H., Yan, W., 2020. CFD-DEM simulation of proppant transport by supercritical $CO_2$ in a vertical planar fracture. J. Nat. Gas Sci. Eng. 84, 103647. https://doi.org/10.1016/j.jngse.2020.103647.